






Evaluation of Fe-nitrides, -borides and -carbides for enhanced magnetic fluid hyperthermia with experimental study of α'' -Fe₁₆N₂ and ϵ -Fe₃N nanoparticles

I Dirba^{1,*} , C K Chandra¹ , Y Ablets¹, J Kohout² , T Kmječ², O Kaman³ 
and O Gutfleisch¹ 

¹ Functional Materials, Institute of Materials Science, Technical University of Darmstadt, Alarich-Weiss-Straße 16, 64287 Darmstadt, Germany

² Faculty of Mathematics and Physics, Charles University in Prague, V Holešovičkách 2, 180 00 Praha 8, Czech Republic

³ FZU—Institute of Physics of the Czech Academy of Sciences, Cukrovarnická 10, 162 00 Praha 6, Czech Republic

E-mail: imants.dirba@tu-darmstadt.de

Received 5 August 2022, revised 25 October 2022

Accepted for publication 7 November 2022

Published 17 November 2022



CrossMark

Abstract

In this work, we investigate alternative materials systems that, based on their intrinsic magnetic properties, have the potential to deliver enhanced heating power in magnetic fluid hyperthermia. The focus lies on systems with high magnetization phases, namely iron-nitrogen (Fe-N), iron-boron (Fe-B) and iron-carbon (Fe-C) compounds, and their performance in comparison to the conventionally used iron oxides, γ -Fe₂O₃, Fe₃O₄ and non-stoichiometric mixtures thereof. The heating power as a function of the applied alternating magnetic field frequency is calculated and the peak particle size with the maximum specific loss power (SLP) for each material is identified. It is found that lower anisotropy results in larger optimum particle size and more tolerance for polydispersity. The effect of nanoparticle saturation magnetization and anisotropy is simulated, and the results show that in order to maximize SLP, a material with high magnetization but low anisotropy provides the best combination. These findings are juxtaposed with experimental results of a comparative study of iron nitrides, namely α'' -Fe₁₆N₂ and ϵ -Fe₃N nanoparticles, and model nanoparticles of iron oxides. The former ones are studied as heating agents for magnetic fluid hyperthermia for the first time.

Supplementary material for this article is available [online](#)

Keywords: magnetic fluid hyperthermia, power dissipation, iron nitrides, iron borides, iron carbides, iron oxides, Mössbauer spectroscopy

(Some figures may appear in colour only in the online journal)

* Author to whom any correspondence should be addressed.



Original content from this work may be used under the terms of the [Creative Commons Attribution 4.0 licence](#). Any further distribution of this work must maintain attribution to the author(s) and the title of the work, journal citation and DOI.

1. Introduction

The survival rate of mammalian cells decreases drastically at $T \geq 43$ °C [1], which opens the door for employing hyperthermic effects as a therapeutic tool in cancer treatment by raising the temperature of tumor tissue [2]. This can be done as a stand-alone technique or to enhance the efficiency of chemo- and radiation treatments [3–5]. Moreover, magnetic fluid hyperthermia (MFH) using magnetic nanoparticles that produce heat in response to an applied alternating magnetic field (AMF) has the potential to deliver targeted treatment, focusing the energy source to achieve doses that are selectively localized within the tumor volume [6]. Various clinical studies have already demonstrated the potential of this method [7–10].

Typically, superparamagnetic iron oxide nanoparticles, e.g. γ - Fe_2O_3 (maghemite), Fe_3O_4 (magnetite) and their mixtures are used in MFH [6–9, 11–13], as they are inexpensive to produce, chemically stable, show low toxicity and their pathways of metabolism are known [8]. Because of their ferrimagnetic nature, the saturation magnetization remains moderate (see the overview of selected materials in table 1, including novel and potentially promising heating agents). It has been shown that individual nanoparticles cannot deliver a sufficient heating effect due to their high surface-area-to-volume ratio, which results in rapid heat dissipation [14–16]. This is particularly important for applications where the concentration is very low, for instance in the case of targeted hyperthermia [17] where the main challenge is to obtain sufficiently high concentrations of nanoparticles in the cancer cells resulting in sufficient heating at clinically tolerable levels of AMF [18]. Furthermore, to treat smaller tumors (larger thermal losses into surroundings due to their higher surface-area-to-volume ratio) and reduce the necessary dose of the heating agent, enhanced specific loss power (SLP) values are crucial in order to achieve the desired effect (the quantity is traditionally denoted as SAR, i.e. specific absorption rate although SAR *sensu stricto* is defined as energy absorbed per unit mass of tissue (more detailed discussion can be found for example in [19–21])). For example, an SLP of more than 1 kW g^{-1} is predicted to be necessary for treatment of a tumor with the size of about 3 mm, and an SLP of 10 kW g^{-1} in the case of targeted particle delivery when reaching concentrations of 1 mg ml^{-1} [14]. To summarize, a novel magnetic material with superior magnetic properties enabling enhanced heating power would be highly beneficial.

The goal of the present work is therefore to consider alternative material systems and identify the most promising candidates that possess favorable magnetic properties for significantly enhanced heating power. For a qualitative comparison between the different materials, the heating power of nanoparticles is calculated and the optimum particle size is identified. Several systems with potentially promising phases are investigated, namely iron-nitrogen (Fe-N), iron-boron (Fe-B) and iron-carbon (Fe-C) compounds, and

compared to the conventional iron oxides. In the following part, the conclusions are supplemented by an experimental study on magnetic nanoparticles of two selected iron nitrides, namely α'' - Fe_{16}N_2 and ε - Fe_3N , and model iron oxides.

The fascinating phase diagram of iron nitrides provides—at least at first glance—very attractive systems with respect to the development of nanocrystalline forms for medical applications, like magnetic fluid hyperthermia. Specifically, the Fe-N phases with nitrogen content up to 25 at% exhibit ferromagnetic ordering at room temperature characterized by high saturation magnetization, the iron nitrides are expected to be rather biocompatible/non-toxic considering the constituting elements, and their nanoparticles are also less sensitive to oxidation by air compared to metal Fe nanoparticles. Nevertheless, the synthesis of iron nitride nanoparticles is challenging, even cumbersome and definitely not as straightforward as the preparation of simple iron oxides or ferrites [22, 23]. The experimental part of the present study employs well-defined samples of α'' - Fe_{16}N_2 and ε - Fe_3N nanoparticles that were prepared in our laboratory with a decent yield. The interstitial compound ε - Fe_3N (space groups $P6_3/mmc$, $P6322$, or $P312$) is structurally derived from the hexaferrum, ε -Fe, with the hexagonal close-packed arrangement of Fe atoms, where N atoms occupy in an ordered way one third of octahedral interstices. The tetragonal crystal structure of α'' - Fe_{16}N_2 ($I4 \text{ mmm}^{-1}$) is based on the body-centered cubic (bcc) α -Fe, whose eight unit cells are supplemented just by two N atoms in octahedral interstices.

2. Mathematical model and numerical framework

Since remanence and coercivity in single-domain particles decrease rapidly with decreasing particle size and vanish near the critical superparamagnetic size, static hysteresis losses become negligible [24, 25] and therefore are not considered in our calculations. Upon a change in the external magnetic field, magnetic moments in a suspension of superparamagnetic particles can reach equilibrium by two relaxation mechanisms, which result in dynamic hysteresis losses due to magnetic relaxation with a phase lag. First, the entire particle can rotate with respect to the surrounding liquid medium. This process is described by the Brownian relaxation time [26]. However, upon administration of nanoparticles into the target tissue, non-specific interactions typically lead to high frictional forces that practically immobilize the particles [27, 28]. Hence, the particles are not able to freely rotate, and the Brownian relaxation can be usually neglected. Therefore, τ_B is not taken into account in the calculations discussed later in this work (explained in more detail in [29]). The other heating process mechanism is the Néel relaxation, i.e. the rotation of magnetization that occurs if the magnetic moment of the particle overcomes the energy barrier due to thermal fluctuations. Since the commonly used magnetic nanoparticles in MFH (the cubic phases Fe_3O_4 and γ - Fe_2O_3) do not possess

Table 1. Saturation magnetization M_s , anisotropy constant K and theoretical density ρ for materials studied in this work, including both conventional and potential heating agents.

Material	M_s (A m ² kg ⁻¹)	K (kJ m ⁻³)	ρ (g cm ⁻³)	References
Fe ₃ O ₄	92	13	5.17	[43]
CoFe ₂ O ₄	81	270	4.9	[43]
Fe ₁₆ N ₂	162	960	7.43	[23, 44]
Fe ₄ N	198	29	7.21	[45, 46]
Fe ₃ N	106	-390	7.20	[47–49]
Fe ₃ C	142	450	7.66	[50]
Fe ₅ C ₂	143	260	7.6	[48, 49, 51]
Fe ₂ B	167	-430	7.33	[52]
Fe ₃ B	175	340	7.3	[53]
Fe	217	48	7.87	[43]
Fe ₆₅ Co ₃₅	240	20	8.11	[54]

uniaxial anisotropy, instead of using the original expression for the relaxation time introduced by Néel [30], the one later derived by Brown for particles with an arbitrary anisotropy is applied [31]:

$$\tau_N = \tau_0 \left(\frac{\varepsilon_B}{k_B T} \right)^{-1/2} e^{\frac{\varepsilon_B}{k_B T}} \quad (1)$$

where the energy barrier $\varepsilon_B = KV$ (K is the anisotropy constant and V particle volume). The pre-exponential factor (attempt time) τ_0 is material-dependent and can be approximated as a function of saturation magnetization and Gilbert damping parameter [32]. To avoid ambiguity in the damping parameter for different materials and to be consistent with previous modelling works [14, 33, 34], the constant attempt time value of $\tau_0 = 10^{-9}$ s is applied.

Since the goal of this study is to qualitatively compare various materials rather than calculate SLP values with the highest possible accuracy, the standard approach [35] has been employed (more quantitative agreement has been achieved by Monte Carlo simulations [36, 37]). For randomly oriented nanoparticles and small applied magnetic fields where the linear response theory (LRT) is valid, the rate of power dissipation per unit volume of particles is expressed as (detailed treatment of the problem can be found for example in [34] or [35]):

$$P_H = \frac{\pi \mu_0^2 M_s^2 V H_0^2}{3k_B T} \frac{f \omega \tau_{\text{eff}}}{1 + (\omega \tau_{\text{eff}})^2} \quad (2)$$

where μ_0 is vacuum permeability, and f are the amplitude and frequency of the applied AMF, τ_{eff} is the effective relaxation time ($\frac{1}{\tau_{\text{eff}}} = \frac{1}{\tau_N} + \frac{1}{\tau_B}$), and $\omega = 2\pi f$ is the angular frequency. The maximum power dissipation and the optimum particle size for each investigated material under various parameters of the applied AMF is solved numerically using equation (2) with relaxation time according to equation (1) by in-house developed framework based on Python JupyterLab [38, 39]. The code with all the functionalities is openly available at the *Technical University of Darmstadt's* institutional repository [29]. It has to be noted that the domain of validity of LRT is limited to low magnetic fields and low particle sizes [35, 40, 41], where magnetization is assumed to be linear for

$\alpha = \frac{\mu_0 M_s V H}{k_B T} < 1$. For the majority of calculations considered in this work, the evaluated optimum particle size lies indeed in this range. Moreover, it has been shown experimentally on magnetite Fe₃O₄ nanoparticles that even for $\alpha > 1$ the optimum particle size is close to that calculated by LRT [42].

The most commonly used experimental quantity for characterization of the MFH heating performance is the SLP. To be able to compare the calculated P_H values with those measured experimentally, the heating power is normalized by the density of the heating agent material.

In this work, alternative materials systems that, based on their intrinsic magnetic properties (K and M_s), have the potential to deliver enhanced heating power for MFH are investigated and compared to the traditionally used iron oxides. All the materials used in the calculations with their corresponding properties are summarized in table 1.

3. Results and discussion

3.1. Optimum particle size and magnetic properties

The calculated SLP curves as a function of particle size for different materials with the properties given in table 1 are shown in figure 1. This graph vividly illustrates the significance of both the intrinsic magnetic properties of the material and the particle size. There is a sharp maximum in SLP for each material in agreement with the previous modelling and experimental results [34, 55]. The position of the maxima depends inversely on the corresponding anisotropy constant and shifts to a larger particle size with lower K . As the result, the feasibility of high anisotropy materials such as Fe₁₆N₂ for MFH applications becomes very challenging since very fine nanoparticles with a diameter of ≈ 4 nm and narrow size distribution would need to be produced, which in practice is very difficult. Moreover, high K materials generally show larger coercivities due to the increased anisotropy field, which, as already pointed out by Dutz and Hergt [33], presents another obstacle because the applied magnetic field amplitude should exceed the coercivity of the particles to obtain maximum power loss. Yet, the available magnetic field amplitudes in MFH are clearly limited. Another important point here is that

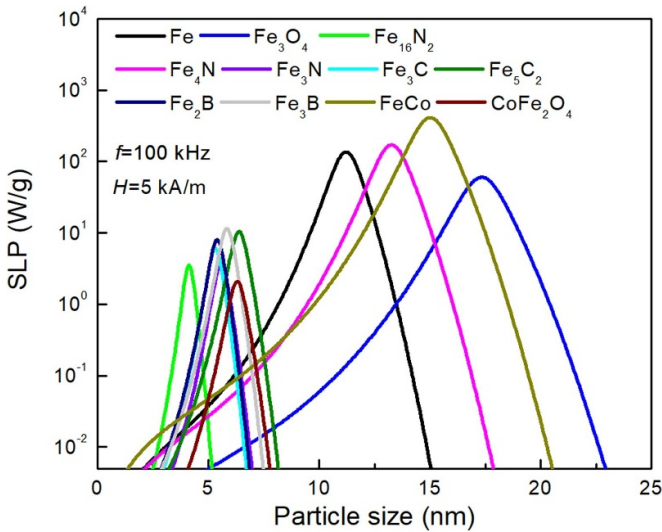


Figure 1. Calculated SLP values as a function of particle size for materials given in table 1 for $f = 100$ kHz and $H = 5$ kA m⁻¹ under the condition of the LRT validity.

the lower the anisotropy constant, the broader the peak in SLP, and thus larger polydispersity can be tolerated, which again is very important when the actual synthesis of nanoparticles is considered.

Examination of equation (2) suggests several options for increasing the rate of power dissipation solely from the mathematical point of view. First, P_H could be increased by simply using higher applied magnetic field amplitude and frequency. However, as already discussed, the product $f \cdot H = 4.85 \cdot 10^8$ A (m·s)⁻¹ is the limiting factor for this approach. Second, since P_H scales with M_s , an increase in nanoparticle magnetization above the conventionally used iron oxides would be highly beneficial. Several Fe nitrides, carbides and borides, as well as metal Fe and Fe-Co, seem to be promising, taking into account their high magnetization at room temperature (see table 1). Nevertheless, the development of an efficient heating agent based on these phases is not that straightforward. This is revealed by figure 1 and evidenced by figure 2, which shows the dependence of the maximum SLP (for an optimum particle size according to figure 1) on the saturation magnetization. The common magnetite shows superior SLP compared to most of the iron nitride, carbide, and boride phases despite its much lower magnetization. The reason for this can be found in the third factor contributing to the heating power according to equation (2), namely in the particle volume V , which increases as d_p^3 . Consequently, the larger the optimum (peak) particle size (corresponding to the peak in SLP), the better is the respective material for achieving a high heating efficiency. In conclusion and in agreement with previous calculations [40], material with high magnetization but low anisotropy provides the best combination to maximize the heating effect.

3.2. Materials optimization approach

The last conclusion of the previous section is of great importance and shows that the materials science approach,

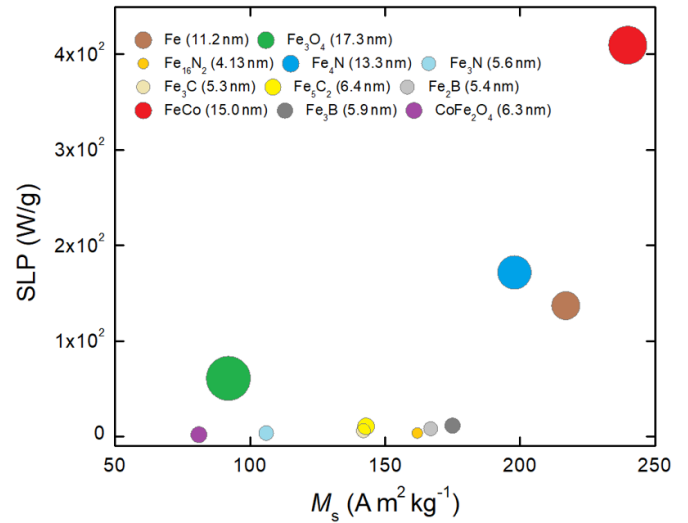


Figure 2. Calculated SLP values (under the condition of the LRT validity) as a function of saturation magnetization for materials described in table 1. Sizes of the circles represent the relative particle diameters for the maximum SLP according to figure 1. Actual values of the particle diameters are given in the parentheses in the legend.

where the target composition of a particular material is rationally designed to meet the desired criteria—maximum magnetization with minimum anisotropy, provides a promising path towards maximizing SLP in magnetic fluid hyperthermia. Several studies have been conducted, for example, on nanoparticles of metal iron and iron carbide nanoparticles [56, 57], but as far as we have been able to ascertain, iron nitride and iron boride systems have never been explored in this respect.

It has been shown both experimentally and by density functional theory calculations that the magnetocrystalline anisotropy of iron nitrides can be tuned by adjusting the nitrogen content, which determines the anisotropic crystal lattice expansion from the bcc arrangement in α -Fe to the body-centered tetragonal in α'' -Fe₁₆N₂ [58–60]. The degree of ordering of the N atoms also plays role in the resultant values of saturation magnetization and anisotropy constant [61, 62]. However, these effects result in an enhanced magnetocrystalline anisotropy of Fe₈N_x. The cubic γ' -Fe₄N phase [45] with high magnetization and low anisotropy is likely to be a more suitable candidate as is also evidenced from the reasonable SLP performance in figures 1 and 2. Additional important factor in favor of γ' -Fe₄N is the chemical stability. The α'' -Fe₁₆N₂ phase appears to be metastable and unless passivated on the surface or coated with a protective layer, it is prone to oxidation [23, 63].

In the iron-boron system, magnetocrystalline anisotropy can be tuned by Co doping [52, 64]. The complex dependence of magnetocrystalline anisotropy energy on the Co content together with the change in the magnetic moment of the phase is illustrated in figure 3. The binary Fe₂B has a negative K (easy-plane anisotropy), which increases with x in (Fe_{1-x}Co_x)₂B, reaching 494 kJ m⁻³ for $x = 0.25$, and decreases again for higher Co contents [65]. Magnetic moment

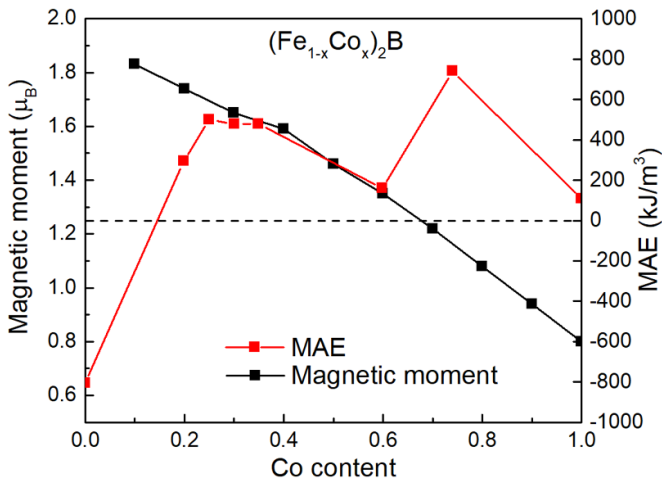


Figure 3. Saturation magnetic moment per magnetic atom and magnetocrystalline anisotropy energy (MAE) for $(\text{Fe}_{1-x}\text{Co}_x)_2\text{B}$ systems (data from [65, 66]). Lines are provided as a guide for the eye.

decreases monotonously with increasing Co content. By adjusting the Co content close to the zero magnetocrystalline anisotropy crossover points, it is possible to obtain a very low anisotropy material.

The binary iron-cobalt system is of great interest due to its high magnetization. Also, in this case, both magnetization and anisotropy can be tuned by varying the chemical composition. The anisotropy becomes almost zero at around 40–50 wt.% Co depending on the degree of ordering [67]. However, the presence of Co in the heating agent may represent an obstacle for application in MFH due to the toxicity of its ions. Even if such magnetic particles are coated by a robust shell that prevents any leaching of metal ions under physiological conditions, the presence of this metal as such may hinder the development due to toxicity concerns and risks related to clinical studies.

To conclude, it appears feasible to engineer by interstitial or substitutional alloying various Fe-based materials with high magnetization towards a low anisotropy for enhanced SLP in magnetic fluid hyperthermia, thus advancing beyond the conventionally used iron oxides. Obviously, in addition to magnetic properties and heating power, detailed studies addressing their chemical stability and biocompatibility of the potential heating agents will be necessary.

4. Experimental study on selected iron nitrides

4.1. Experimental details

High phase-purity $\alpha''\text{-Fe}_{16}\text{N}_2$ nanoparticles used in this study have been produced via a novel two-step route established by Dirba *et al* [23]. First, commercial $\gamma\text{-Fe}_2\text{O}_3$ nanoparticles with an average particle size of 20–40 nm were reduced to $\alpha\text{-Fe}$ in high-pressure hydrogen [68]. In the second step, the resulting $\alpha\text{-Fe}$ nanoparticles were nitrogenated in an ammonia flow to produce the iron nitride.

Monodisperse $\varepsilon\text{-Fe}_3\text{N}$ nanoparticles were synthesized via the wet-chemical procedure described by Hijikata *et al* [69]. In short, $\text{Fe}(\text{CO})_5$ was thermally decomposed in a three-neck round-bottom flask filled with kerosene as an inert high-boiling solvent and a mixture of succinimide and oleylamine as a surfactant. Ammonia gas was passed through the carrier reaction mixture, which was continuously stirred with a magnetic stirrer. The obtained nanoparticles were washed by petroleum ether/ethanol mixtures, dried and dispersed in hexane for heating rate measurements.

Magnetic measurements were performed at room temperature by using the vibrating sample magnetometer (VSM) (7400 Series, Lake Shore) and a Quantum Design Physical Property Measurement System with a VSM option. Powder diffractometer STOE Stadi P (Mo $\text{K}_{\alpha 1}$ -radiation, $\lambda = 0.70930 \text{ \AA}$) was used for collecting x-ray diffraction (XRD) data. Transmission electron microscopy (TEM) was done with a FEI CM20 ST microscope operated at an acceleration voltage of 200 kV. The samples were drop-cast onto carbon-coated copper grids. An alternating current (AC) magnetic field applicator (DM100 series, nB nanoScale Biomagnetics) with a vacuum-insulated calorimeter and an optical fiber temperature probe (see schematic in the supplementary material) immersed in the middle of the dispersions in hexane was used for the heating rate measurements in AMF with an amplitude of $H = 19.9 \text{ kA m}^{-1}$ and frequency of $f = 402 \text{ kHz}$.

The ^{57}Fe Mössbauer spectra were collected in transmission geometry using a constant-acceleration spectrometer equipped with a $^{57}\text{Co}/\text{Rh}$ source. The spectra of powdered samples sealed in glass ampules and samples mixed with tableting wax and pressed into pellets in a nitrogen atmosphere provided practically identical relative intensities of individual components in the spectra. Therefore, only the spectra of pellets, which have a higher signal-to-noise ratio, are presented and discussed below. The calibration of the spectrometer and determination of isomer shifts were performed with respect to a room-temperature Mössbauer spectrum of an $\alpha\text{-Fe}$ foil. The spectra were acquired at room temperature and 4.2 K, the in-field spectra were measured at 4.2 K in the magnetic field of 4.775 MA m^{-1} oriented perpendicularly to the direction of the γ -rays. The spectra were evaluated by using the current version of the Confit[®] [70] program. The room-temperature Mössbauer spectra contain a small doublet component denoted as D, which originates from the experimental setup, namely the Fe impurity in the Al foil of the detector.

The intrinsic or applied magnetic fields acting on the ^{57}Fe nucleus split its Mössbauer spectrum into a sextet. The ratio of intensities I_i of lines i in the sextet depends on the angle θ_m between the direction of the effective magnetic field at the nucleus and the propagation direction of the γ -rays as [71]

$$I_{1,6} : I_{2,5} : I_{3,4} = 3 : b_S : 1, \quad b_S = 4\sin\theta_m / (1 + \cos^2\theta_m). \quad (3)$$

The value $b_S = 2$ of the fitted sextet corresponds to a random orientation of the magnetic moments of the Fe atoms in the powder sample. Further, in the first-order approximation, the quadrupole shift QS depends on the polar θ and azimuthal

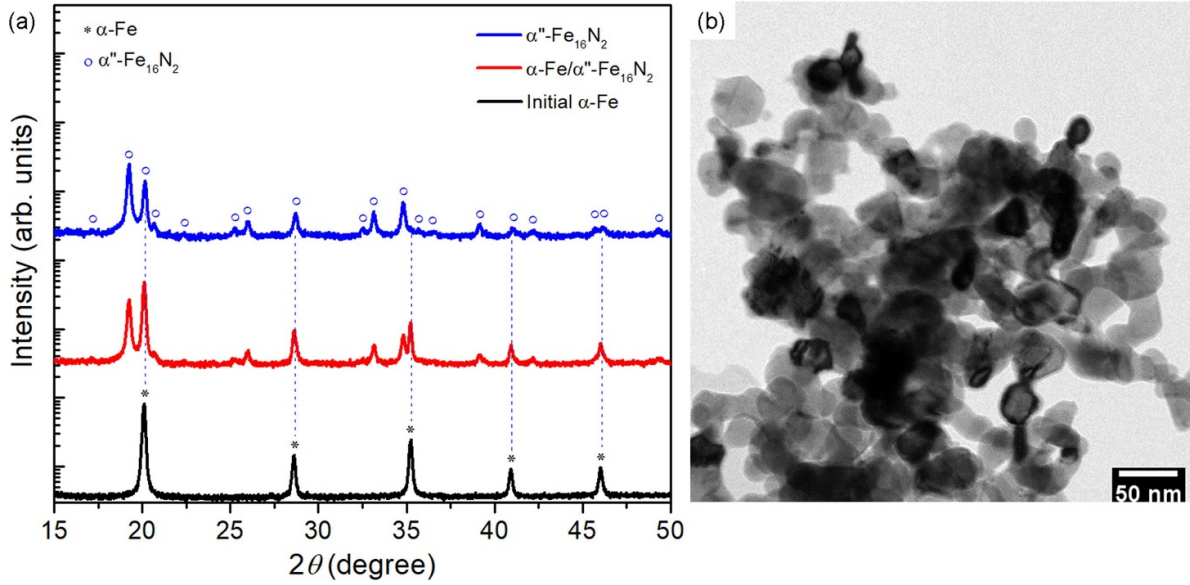


Figure 4. (a) XRD patterns of the initial α -Fe, partially nitrided α -Fe/ α'' -Fe₁₆N₂ sample and fully nitrided α'' -Fe₁₆N₂ nanoparticles. (b) Bright-field TEM image of the final α'' -Fe₁₆N₂ product.

φ angles between the principal axis of the electric field gradient (EFG) tensor and the direction of the hyperfine magnetic field B_{hf} [72] as:

$$QS = \frac{1}{4}eQV_{zz}(3\cos^2\theta - 1 + \eta\sin^2\theta\cos 2\varphi), \quad (4)$$

where e is the electron charge, Q is the quadrupole moment of ^{57}Fe nuclei in the excited state with spin $I = 3/2$, V_{zz} is the main component of the EFG tensor and η is the asymmetry parameter.

4.2. Experimental results

4.2.1. α'' -Fe₁₆N₂ nanoparticles.

Since there has been controversy about the magnetic properties and stability of the α'' -Fe₁₆N₂ phase, we combined XRD measurements with detailed Mössbauer spectroscopy investigations to shed more light on the phase purity and possible oxidation of the synthesized samples that would alter their magnetic properties and thus the MFH heating performance. We examined three samples at different process stages, the corresponding XRD patterns are shown in figure 4. The initial hydrogen-reduced nanoparticles (bottom) show only α -Fe diffraction peaks (PDF card No.: 00-006-0696). The intermediate partially nitrided sample (middle) shows a mixture of α -Fe/ α'' -Fe₁₆N₂. The fully nitrided sample (top) shows diffraction lines only of the α'' -Fe₁₆N₂ phase (PDF card No.: 01-078-1865). The average particle size of the nitrided samples is $47 \text{ nm} \pm 5 \text{ nm}$ according to TEM analysis (see illustrative micrograph in figure 4(b)).

However, the analysis of XRD data might not precisely reveal the phase fractions due to amorphization, which might have resulted from the hydrogen absorption-desorption processes as well as low-temperature nitriding. Therefore, ^{57}Fe

Mössbauer spectroscopy was crucial for the analysis since this method using ^{57}Fe nuclei as local probes in the material does not require long-range order.

The ^{57}Fe Mössbauer spectra of α -Fe nanoparticles depicted in figures 5(a)–(c) indicate that the core of the nanoparticles formed by α -Fe [73] (relative area in the spectrum $A = 83(1)\%$) was surrounded by an oxidized layer ($A = 16(1)\%$), which undergoes superparamagnetic (SP) relaxation at room temperature (M-SP component) with a frequency comparable to the Mössbauer time scale of $\sim 10^{-7}$ s. By assuming the identical Lamb-Mössbauer factors in all Fe positions, the relative areas of individual components roughly correspond to the relative number of Fe atoms in the respective sites.

Due to the detection of localized divalent iron in octahedral positions (isomer shift $\delta \sim 1.1 \text{ mm s}^{-1}$) [74] in the sample at liquid helium temperature, we conclude that the oxide phase in the shell is nonstoichiometric magnetite (Fe^{3+})[$\text{Fe}^{2+}_{1-3\delta}\text{Fe}^{3+}_{1+2\delta}\square_{\delta}$] O_3 , where \square dex an iron vacancy, $()$ tetrahedral and $[\]$ octahedral sites of the spinel structure. When the external magnetic field was applied, the effective magnetic field on the ^{57}Fe nuclei $B_{\text{eff}} = |B_{\text{ext}} + B_{\text{hf}}|$ of the α -Fe decreased from 34 T ($B_{\text{ext}} = 0$ T) to 28.4 T ($B_{\text{ext}} = 6$ T) because the hyperfine magnetic field at the nucleus is antiparallel to the direction of the magnetic moment of the iron atom. At the same time, the line intensity ratio 3:4:1, see equation (3), suggests that the Fe magnetic moments (magnetic moments of ^{57}Fe nuclei) in α -Fe nanoparticles were oriented parallel (antiparallel) to the applied field. In contrast, the line intensity ratio 3:2:1 in sextets of the oxide phase indicates that the Fe magnetic moments in the shell are not oriented in the direction of the external field and probably compensate for the dipolar magnetic field produced by the α -Fe cores. In the external field, the effective field on the ^{57}Fe

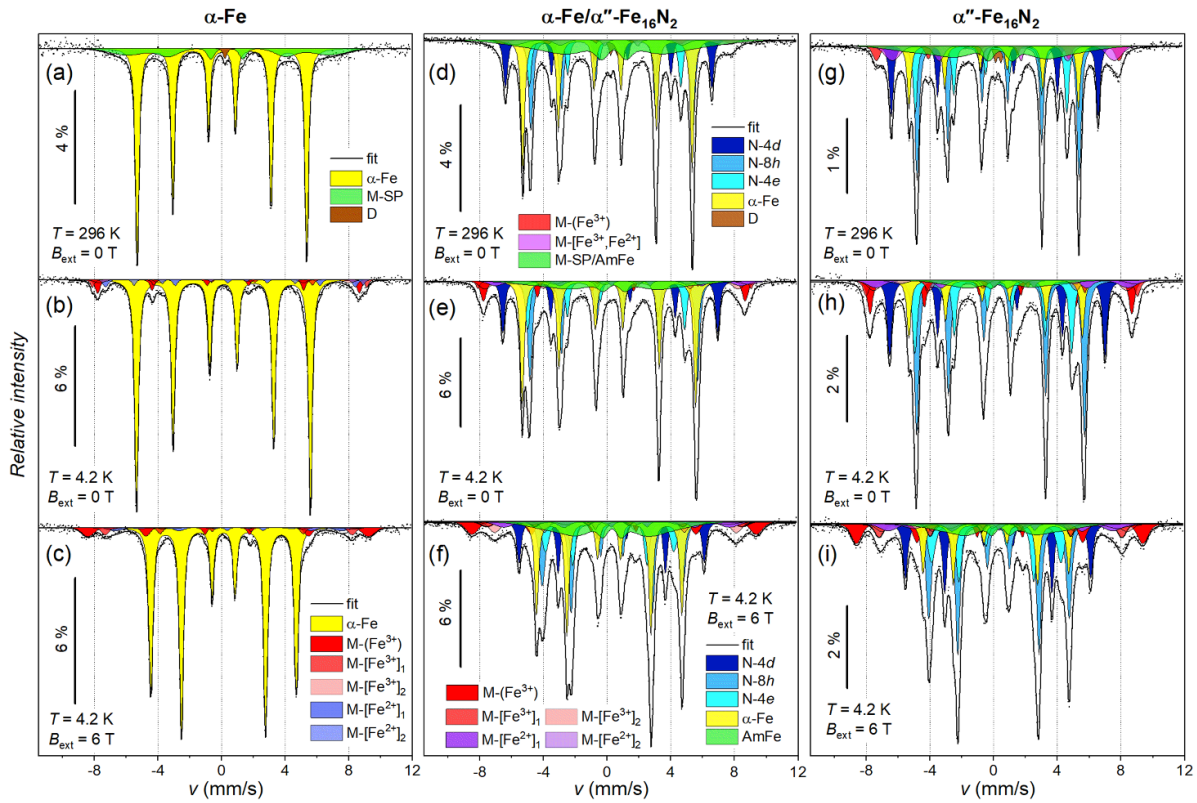


Figure 5. The ^{57}Fe Mössbauer spectra at room temperature (upper row), and at liquid helium temperature at zero field (middle) and at an applied field of 6 T (bottom) of: (a)–(c) initial $\alpha\text{-Fe}$, (d)–(f) partially nitrated $\alpha\text{-Fe}/\alpha''\text{-Fe}_{16}\text{N}_2$ and (g)–(i) fully nitrated $\alpha''\text{-Fe}_{16}\text{N}_2$ nanoparticles. The components labelled by N denote Fe sites of $\alpha''\text{-Fe}_{16}\text{N}_2$, by M the Fe^{2+} and Fe^{3+} sites of nonstoichiometric magnetite, by AmFe a mostly amorphous phase of Fe possibly doped with nitrogen/oxygen, and by D the Fe impurity in the Al-foil of the Mössbauer detector. The legends of the two nitrated samples are identical.

nuclei in the tetrahedral sites of magnetite (sextet $\text{M}(\text{Fe}^{3+})$) increases and in the octahedral sites (sextets $\text{M}[\text{Fe}^{3+}]_{1,2}$ and $\text{M}[\text{Fe}^{2+}]_{1,2}$) decreases, due to the ferrimagnetic ordering of the Fe moments. The hyperfine parameters along with other parameters of the fits are summarized in table S1 in the supplementary material.

The ^{57}Fe Mössbauer spectra of the intermediate product $\alpha\text{-Fe}/\alpha''\text{-Fe}_{16}\text{N}_2$ below the Curie temperature T_C , depicted in figures 5(d)–(f), were fitted with the same components as the final product $\alpha''\text{-Fe}_{16}\text{N}_2$, which will be described below in more detail. Briefly, the sample consisted of $\alpha''\text{-Fe}_{16}\text{N}_2$ (45%), $\alpha\text{-Fe}$ presumably in the core of the particles (26%), magnetite in the shell of the particles (18%), and the remaining 11% is attributed to a disordered phase of iron, presumably containing nitrogen or oxygen. The fitted parameters are provided in table S2 in the supplementary material.

Similarly to the $\alpha\text{-Fe}/\alpha''\text{-Fe}_{16}\text{N}_2$ intermediate, the ^{57}Fe Mössbauer spectra of the final product $\alpha''\text{-Fe}_{16}\text{N}_2$ under the Curie temperature T_C show that the sample is composed of four distinct phases (see spectra in figures 5(g)–(i) and parameters of the fit in table S3 in the supplementary material).

First, the targeted $\alpha''\text{-Fe}_{16}\text{N}_2$ phase contributes to the spectra with three sextets ('N') corresponding to the three inequivalent Fe positions in the $\alpha''\text{-Fe}_{16}\text{N}_2$ tetragonal structure: 4 *d*, 8 *h*, and 4 *e* [75]. The ratio of their respective areas was fixed in the fitting procedure to the ideal ratio 1:2:1, the total content

of the nitride phase was 61%. The hyperfine field of the N-4 *d*, N-8 *h*, and N-4 *e* components at liquid helium temperature, $B_{\text{hf}} = 42.3(2)$, $32.8(2)$, and $30.6(2)$ T, respectively, decreased only by 1–2 T compared to room temperature. In the applied field, the magnetic moments of Fe in all three sites were oriented to the direction of the field, as indicated by the line intensity ratio 3:4:1 of the respective sextets (see equation (3)). Moreover, their quadrupole shifts were averaged over the entire spatial angle to zero in the in-field spectrum because of the random orientation of the grains in the powdered sample, i.e. the random angle between the principal axis of the EFG tensor and the direction of the Fe magnetic moments (magnetic moments of ^{57}Fe nuclei) in the external field (see equation (4)).

The second phase is $\alpha\text{-Fe}$ probably remaining in the core of the nanoparticles (12%). Again, the nanoparticles contain an oxidized surface layer composed of nonstoichiometric magnetite [74, 76] (22%), possibly doped with nitrogen, which is partially superparamagnetic at room temperature (sextet M-SP). The nanoparticles thus possess the core–double-shell structure. The last phase (5%) contributes with a very broad sextet AmFe even at liquid helium temperature at which we do not expect any persisting superparamagnetic relaxation. This sextet with a broad distribution of hyperfine fields and $\langle B_{\text{eff}} \rangle \sim 20$ T was ascribed to a poorly crystallized phase of iron, probably containing nitrogen, eventually oxygen.

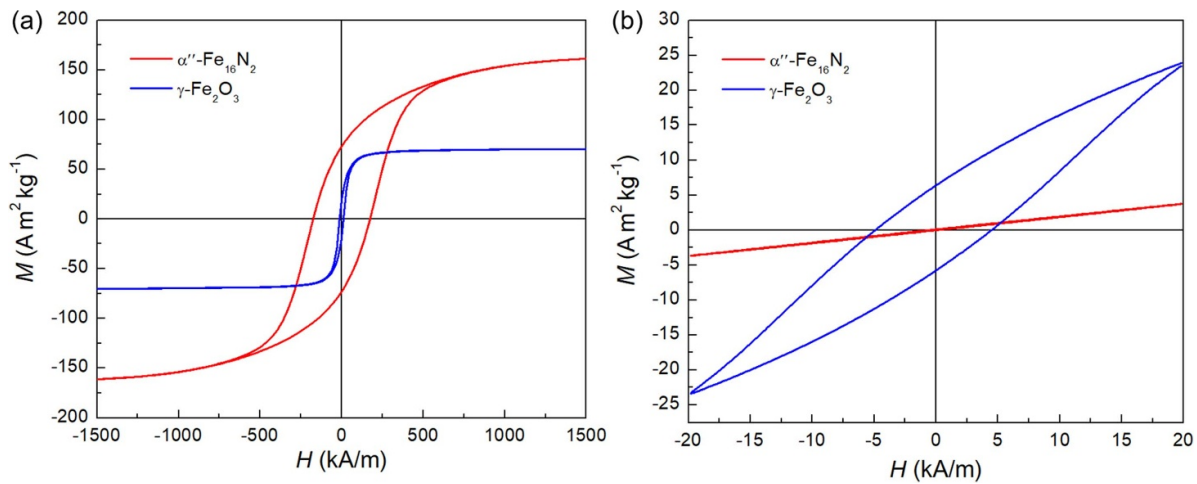


Figure 6. Room temperature VSM $M(H)$ loops for the $\alpha''\text{-Fe}_{16}\text{N}_2$ and $\gamma\text{-Fe}_2\text{O}_3$ nanoparticles.

To conclude, Mössbauer spectroscopy is more accurate for the estimation of $\alpha''\text{-Fe}_{16}\text{N}_2$ phase fraction. The presence of an oxide phase, the nonstoichiometric magnetite in this case, reduces the magnetization of the nanoparticles and thus in addition to N site ordering [61] could be an explanation for the differing values reported in the literature [23, 44]. Whether the observed oxide is remaining from the hydrogen reduction step [68] or originates from the sample oxidation during handling and measurement, remains an open question.

Magnetic properties and MFH heating performance of the prepared $\alpha''\text{-Fe}_{16}\text{N}_2$ nanoparticles with the average particle size around 50 nm were compared to the precursor $\gamma\text{-Fe}_2\text{O}_3$. More details on the synthesis and morphology of the nanoparticles used here can be found in [23, 68]. VSM room temperature hysteresis loops are shown in figure 6. As expected according to table 1, the nitride phase shows significantly higher saturation magnetization in the applied magnetic field of 1500 kA m^{-1} (figure 6(a)). However, much smaller magnetic fields are available for the MFH, therefore supplemental measurements with an applied field of only 19.9 kA m^{-1} were conducted (figure 6(b)). Under these conditions the situation is reversed; $\gamma\text{-Fe}_2\text{O}_3$ nanoparticles demonstrate substantially higher magnetization and a larger area enclosed by their hysteresis loop, whereas $\alpha''\text{-Fe}_{16}\text{N}_2$ particles provide only minor loops.

MFH heating rate measurements were conducted on nanoparticle dispersions in hexane with the concentration of 2 mg ml^{-1} . The results are shown in figure 7, according to which the iron oxide significantly outperforms the nitride under the given conditions. This comparison demonstrates that the saturation magnetization values presented in table 1 alone are not suitable for predicting the heating performance.

Due to the high anisotropy of the $\alpha''\text{-Fe}_{16}\text{N}_2$ phase and low initial susceptibility, the rather small fields available in MFH result in a narrow minor loop of a negligible enclosed area and thus low power losses. If magnetic properties ought to be used for the comparison of different materials, they have to be measured in magnetic fields relevant to MFH. Moreover, only direct current (DC) loops have been considered here although

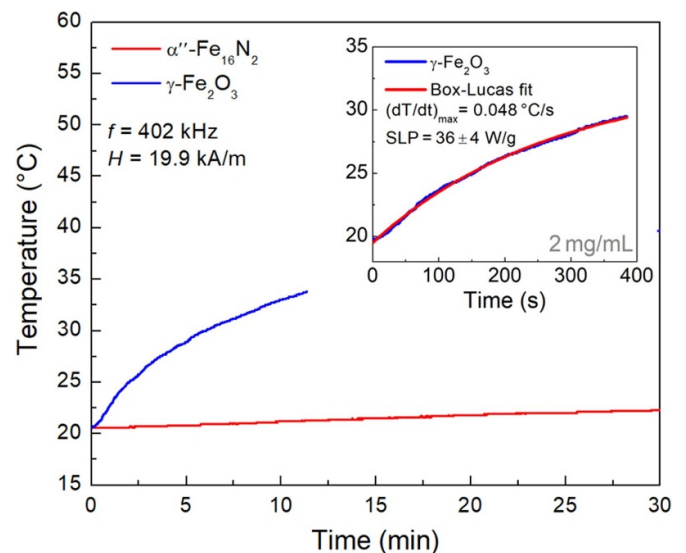


Figure 7. Heating rate measurements for the initial $\gamma\text{-Fe}_2\text{O}_3$ and the fully nitrated $\alpha''\text{-Fe}_{16}\text{N}_2$ nanoparticles suspensions in hexane. Concentration was 2 mg ml^{-1} . The applied AMF amplitude was 19.9 kA m^{-1} and frequency 402 kHz . The inset shows the Box-Lucas fit used to obtain $(dT/dt)_{\text{max}}$ and the corresponding SLP value.

the influence of frequency also plays a significant role and can be assessed by measuring AC hysteresis loops [77].

4.2.2. $\epsilon\text{-Fe}_3\text{N}$ nanoparticles. XRD and TEM characterizations of the $\epsilon\text{-Fe}_3\text{N}$ nanoparticles are provided in figure 8. XRD and selected area electron diffraction patterns depicted in figure 8(a) prove that the sample consists of the single-phase but poorly crystalline $\epsilon\text{-Fe}_3\text{N}$ with no signature of iron oxides admixtures. Bright-field TEM image in figure 8(b) shows that the nanoparticles are monodisperse, exhibit rounded near-spherical shapes with a narrow size distribution and an average particle size of $12.7 \text{ nm} \pm 1.2 \text{ nm}$.

According to TEM analysis the particles exhibit core-shell structure, whose outer regions are less electron-dense than the

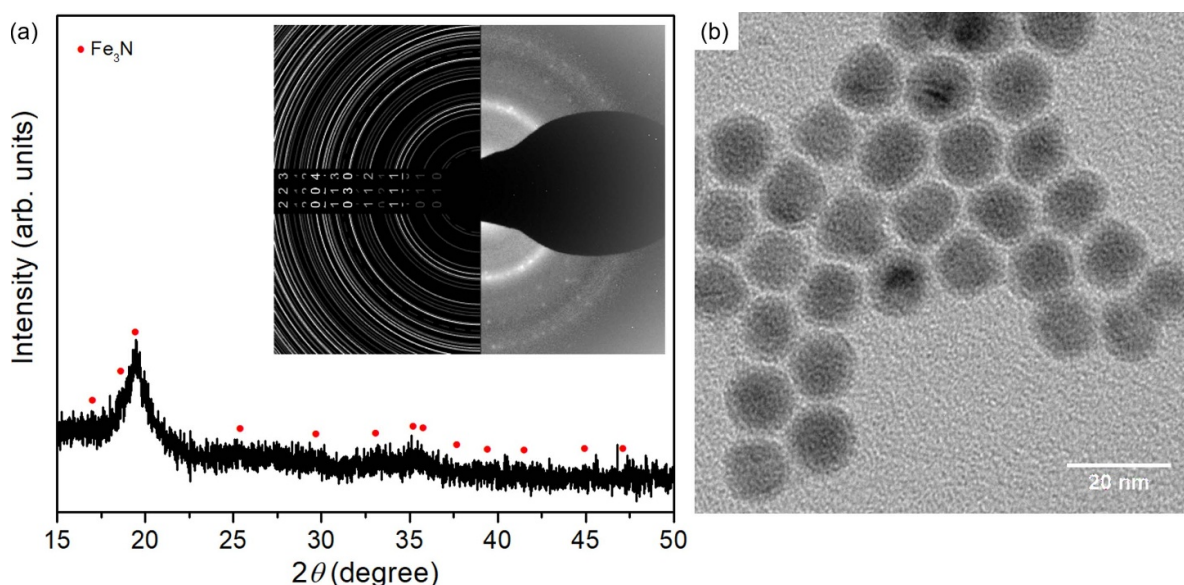


Figure 8. (a) XRD and SAED with the theoretical ring revelation patterns and (b) a bright-field TEM image of ϵ -Fe₃N nanoparticles.

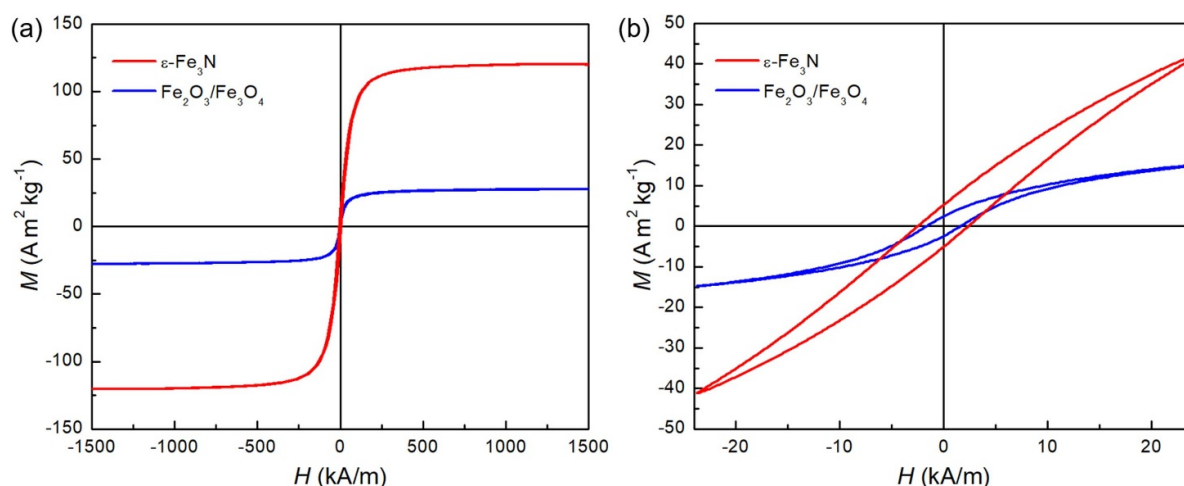


Figure 9. Room-temperature VSM $M(H)$ loops for the ϵ -Fe₃N and Fe₂O₃/Fe₃O₄ nanoparticles in different applied magnetic fields.

core, which can be probably explained in terms of partial surface oxidation. Actually, partial surface oxidation during the sample preparation cannot be ruled out as has been reported previously for larger α'' -Fe₁₆N₂ nanoparticles [23].

VSM room temperature hysteresis loops of ϵ -Fe₃N nanoparticles and comparable Fe₂O₃/Fe₃O₄ (prepared via the same route with comparable particle size and morphology; see figure S1 in the supplementary material) and the ϵ -Fe₃N phase nanoparticles are shown in figure 9. Similarly to α'' -Fe₁₆N₂, the ϵ -Fe₃N phase shows in the applied field of $H = 1500 \text{ kA m}^{-1}$ significantly higher magnetization than the oxide, $120 \text{ A m}^2 \text{ kg}^{-1}$ versus $28 \text{ A m}^2 \text{ kg}^{-1}$ respectively. The values are lower than the bulk ones largely due to presence of residual diamagnetic surfactants (complete removal difficult) and surface effects. In contrast to α'' -Fe₁₆N₂, the ϵ -Fe₃N shows soft magnetic behavior with narrow hysteresis, very low coercivity of $H_c = 4.8 \text{ kA m}^{-1}$ and high initial susceptibility. This results in much higher magnetization also in low applied

fields as shown in figure 9(b). At $H = 23.9 \text{ kA m}^{-1}$, the ϵ -Fe₃N phase has a magnetization of $42 \text{ A m}^2 \text{ kg}^{-1}$ whereas the iron oxide sample shows only $15 \text{ A m}^2 \text{ kg}^{-1}$. Thus, larger power losses are expected in the former case.

MFH heating rate measurements were conducted on nanoparticle dispersions in hexane with the concentration of 2 mg ml^{-1} . The results are shown in figure 10. The step-like curve of the nitride sample in the beginning is caused by the rapid heating rate that exceeds the too-low signal processing rate for temperature readings of the experimental device. In agreement with the magnetization measurements, the ϵ -Fe₃N nanoparticles significantly outperform comparable iron oxide nanoparticles, reaching SLP of $540 \pm 54 \text{ W g}^{-1}$. Actually, temperatures above $60 \text{ }^\circ\text{C}$ are reached within less than two minutes. These first results are promising and illustrate that materials with higher magnetization than the conventional iron oxides, indeed, can be potential candidates for MFH.

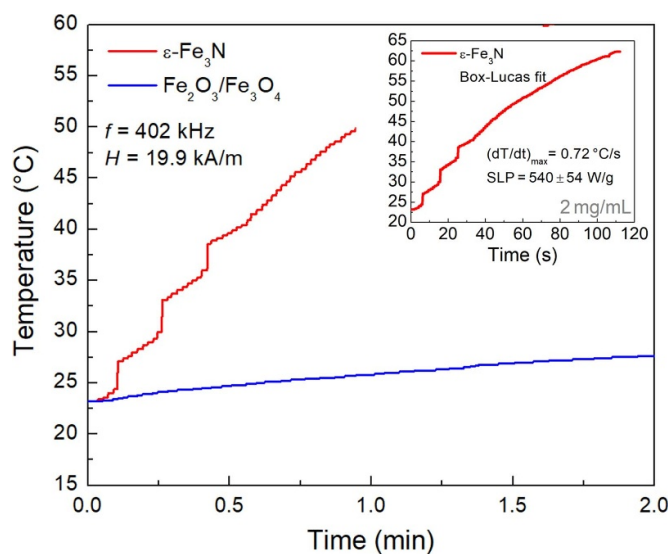


Figure 10. Heating rate measurements for the ε -Fe₃N and Fe₂O₃/Fe₃O₄ nanoparticles suspensions in hexane with the concentration of 2 mg ml⁻¹. The applied AMF amplitude was 19.9 kA m⁻¹ and frequency 402 kHz. The inset shows the Box-Lucas fit used to obtain $(dT/dt)_{\max}$ and the corresponding SLP value.

Further detailed SLP studies in dependence on applied magnetic field parameters as well as studies on the chemical stability of ε -Fe₃N nanoparticles in the biological environment are ongoing.

5. Summary

In this work, we have numerically calculated the maximum power dissipation due to relaxation losses in superparamagnetic nanoparticles by using an in-house developed framework based on Python JupyterLab. Several alternative materials, such as iron-nitrogen (Fe-N), iron-boron (Fe-B), and iron-carbon (Fe-C) systems that, based on their magnetic properties, have the potential to deliver an enhanced heating power for magnetic fluid hyperthermia, were analyzed and compared to the conventionally used iron oxides, Fe₂O₃ and Fe₃O₄.

The main conclusion is that, a material with high magnetization but low anisotropy to achieve large peak SLP particle size provides the best combination. The results show a sharp maximum in SLP for each material whose position depends inversely on the corresponding anisotropy constant and shifts to a larger particle size with lower K . Moreover, the lower the anisotropy constant, the broader the peak in the size dependence of SLP, and thus larger polydispersity can be tolerated, which is important when considering the limits of the size and shape control of the synthesis. This opens the door for a materials science approach where the target composition of the particular material is rationally designed to optimize the intrinsic magnetic properties towards maximizing SLP in magnetic fluid hyperthermia. Interestingly, and perhaps unexpectedly, Fe₂O₃ and Fe₃O₄ phases demonstrate superior SLP

compared to various iron nitride, carbide and boride phases despite their much lower magnetization. The reason lies in the position of their SLP maximum, which is located at larger particle sizes and thereby increases the heating power.

We have also conducted preliminary experimental case studies to test the MFH heating performance for proposed nanoparticles with higher magnetization. Iron nitride α'' -Fe₁₆N₂ and ε -Fe₃N nanoparticles were compared with iron oxides of similar particle sizes. The results show that high anisotropy of the α'' -Fe₁₆N₂ phase is detrimental and results in low initial susceptibility with narrow minor loops with a negligible enclosed area, and thus low power losses in magnetic fields employed for MFH. In contrast, the ε -Fe₃N phase with much lower anisotropy shows very promising heating performance with SLP of 540 ± 54 W g⁻¹ and will be studied further, including also the γ -Fe₄N phase. In addition, other biomedical applications where enhanced magnetization is beneficial for performance, such as magnetic separation, drug and gene delivery, magnetic resonance imaging or magnetic particle imaging should be considered.

Data availability statement

All data that support the findings of this study are included within the article (and any supplementary files).

Acknowledgments

We acknowledge funding by the Deutsche Forschungsgemeinschaft (DFG, German Research Foundation), Project ID Nos. 471878653, 405553726-TRR 270 and CRC 1487. J K and O K are grateful to the Czech Science Foundation (Project No. 22-10035K) and O K is grateful also to the Operational Programme Research, Development and Education financed by European Structural and Investment Funds and the Czech Ministry of Education, Youth and Sports (Project No. SOLID21—CZ.02.1.01/0.0/0.0/16_019/0000760). We would like to thank also to our colleagues Dr Lenka Kubíčková and Dr Karel Závěta for their help during writing and editing the manuscript.

ORCID iDs

I Dirba <https://orcid.org/0000-0002-5335-2152>
 C K Chandra <https://orcid.org/0000-0001-7957-8291>
 J Kohout <https://orcid.org/0000-0002-0708-1494>
 O Kaman <https://orcid.org/0000-0003-1480-2904>
 O Gutfleisch <https://orcid.org/0000-0001-8021-3839>

References

- [1] Hahn G M 1984 Hyperthermia for the engineer: a short biological primer *IEEE Trans. Biomed. Eng.* **31** 3–8
- [2] Wust P, Hildebrandt B, Sreenivasa G, Rau B, Gellermann J, Riess H, Felix R and Schlag P 2002 Hyperthermia in combined treatment of cancer *Lancet Oncol.* **3** 487–97

- [3] Bull J M 1984 An update on the anticancer effects of a combination of chemotherapy and hyperthermia *Cancer Res.* **44** 4853s–6s
- [4] Cavaliere R, Ciocatto E C, Giovanella B C, Heidelberger C, Johnson R O, Margottini M, Mondovi B, Moricca G and Rossi-Fanelli A 1967 Selective heat sensitivity of cancer cells. Biochemical and clinical studies *Cancer* **20** 1351–81
- [5] LeVeen H H, Ahmed N, Piccone V A, Shugaar S and Falk G 1980 Radio-frequency therapy: clinical experience *Ann. New York Acad. Sci.* **335** 362–71
- [6] Gilchrist R K, Medal R, Shorey W D, Hanselman R C, Parrott J C and Taylor C B 1957 Selective inductive heating of lymph nodes *Ann. Surg.* **146** 596–606
- [7] Johannsen M, Gneveckow U, Eckelt L, Feussner A, Waldöfner N, Scholz R, Deger S, Wust P, Loening S A and Jordan A 2005 Clinical hyperthermia of prostate cancer using magnetic nanoparticles: presentation of a new interstitial technique *Int. J. Hyperth.* **21** 637–47
- [8] Thiesen B and Jordan A 2008 Clinical applications of magnetic nanoparticles for hyperthermia *Int. J. Hyperth.* **24** 467–74
- [9] Maier-Hauff K, Ulrich F, Nestler D, Niehoff H, Wust P, Thiesen B, Orawa H, Budach V and Jordan A 2011 Efficacy and safety of intratumoral thermotherapy using magnetic iron-oxide nanoparticles combined with external beam radiotherapy on patients with recurrent glioblastoma multiforme *J. Neurooncol.* **103** 317–24
- [10] Maier-Hauff K et al 2007 Intracranial thermotherapy using magnetic nanoparticles combined with external beam radiotherapy: results of a feasibility study on patients with glioblastoma multiforme *J. Neurooncol.* **81** 53–60
- [11] Laurent S, Dutz S, Häfeli U O and Mahmoudi M 2011 Magnetic fluid hyperthermia: focus on superparamagnetic iron oxide nanoparticles *Adv. Colloid Interface Sci.* **166** 8–23
- [12] Jordan A, Wust P, Scholz R, Tesche B, Fählung H, Mitrovics T, Vogl T, Cervós-Navarro J and Felix R 1996 Cellular uptake of magnetic fluid particles and their effects on human adenocarcinoma cells exposed to AC magnetic fields *in vitro* *Int. J. Hyperth.* **12** 705–22
- [13] Matsumine A, Takegami K, Asanuma K, Matsubara T, Nakamura T, Uchida A and Sudo A 2011 A novel hyperthermia treatment for bone metastases using magnetic materials *Int. J. Clin. Oncol.* **16** 101–8
- [14] Hergt R and Dutz S 2007 Magnetic particle hyperthermia—biophysical limitations of a visionary tumour therapy *J. Magn. Magn. Mater.* **311** 187–92
- [15] Rabin Y 2002 Is intracellular hyperthermia superior to extracellular hyperthermia in the thermal sense? *Int. J. Hyperth.* **18** 194–202
- [16] Koblinski P, Cahill D G, Bodapati A, Sullivan C R and Taton T A 2006 Limits of localized heating by electromagnetically excited nanoparticles *J. Appl. Phys.* **100** 054305
- [17] Suzuki M, Shinkai M, Kamihira M and Kobayashi T 1995 Preparation and characteristics of magnetite-labelled antibody with the use of poly(ethylene glycol) derivatives *Biotechnol. Appl. Biochem.* **21** 335–45
- [18] Pankhurst Q A, Thanh N K T, Jones S K and Dobson J 2009 Progress in applications of magnetic nanoparticles in biomedicine *J. Phys. D: Appl. Phys.* **42** 224001
- [19] Wildeboer R R, Southern P and Pankhurst Q A 2014 On the reliable measurement of specific absorption rates and intrinsic loss parameters in magnetic hyperthermia materials *J. Phys. D: Appl. Phys.* **47** 495003
- [20] Makridis A, Curto S, Van Rhooen G C, Samaras T and Angelakeris M 2019 A standardisation protocol for accurate evaluation of specific loss power in magnetic hyperthermia *J. Phys. D: Appl. Phys.* **52** 255001
- [21] Makridis A, Kazeli K, Kyriazopoulos P, Maniotis N, Samaras T and Angelakeris M 2022 An accurate standardization protocol for heating efficiency determination of 3D printed magnetic bone scaffolds *J. Phys. D: Appl. Phys.* **55** 435002
- [22] Wu K, Liu J, Saha R, Ma B, Su D, Chugh V K and Wang J-P 2021 Stable and monodisperse iron nitride nanoparticle suspension for magnetic diagnosis and treatment: development of synthesis and surface functionalization strategies *ACS Appl. Nano Mater.* **4** 4409–18
- [23] Dirba I, Schwöbel C A, Diop L V B, Duerrschabel M, Molina-Luna L, Hofmann K, Komissinskiy P, Kleebe H J and Gutfleisch O 2017 Synthesis, morphology, thermal stability and magnetic properties of α'' -Fe₁₆N₂ nanoparticles obtained by hydrogen reduction of γ -Fe₂O₃ and subsequent nitrogenation *Acta Mater.* **123** 214–22
- [24] Bean C P and Livingston J D 1959 Superparamagnetism *J. Appl. Phys.* **30** S120–9
- [25] Bean C P 1955 Hysteresis loops of mixtures of ferromagnetic micropowders *J. Appl. Phys.* **26** 1381–3
- [26] MacDougall F H 1946 *Kinetic Theory of Liquids* (London: Oxford University Press)
- [27] Dutz S, Kettering M, Hilger I, Müller R and Zeisberger M 2011 Magnetic multicore nanoparticles for hyperthermia influence of particle immobilization in tumour tissue on magnetic properties *Nanotechnology* **22** 265102
- [28] Richter H, Kettering M, Wiekhorst F, Steinhoff U, Hilger I and Trahms L 2010 Magnetorelaxometry for localization and quantification of magnetic nanoparticles for thermal ablation studies *Phys. Med. Biol.* **55** 623–33
- [29] Dirba I, Chandra C K and Gutfleisch O n.d. Modelling of alternative materials for enhanced magnetic fluid hyperthermia (available at: <https://tudatalib.ulb.tu-darmstadt.de/handle/tudatalib/2625>)
- [30] Neel L 1949 Influence des fluctuations thermiques sur l'aimantation de grains ferromagnétiques très fins *C. R. Hebd. Seances Acad. Sci.* **228** 664–6
- [31] Brown W F 1959 Relaxational behavior of fine magnetic particles *J. Appl. Phys.* **30** S130–2
- [32] Shliomis M I 1974 Magnetic fluids *Sov. Phys.-Usp.* **17** 153–69
- [33] Dutz S and Hergt R 2014 Magnetic particle hyperthermia a promising tumour therapy? *Nanotechnology* **25** 452001
- [34] Rosensweig R E 2002 Heating magnetic fluid with alternating magnetic field *J. Magn. Magn. Mater.* **252** 370–4
- [35] Krishnan K M 2016 *Fundamentals and Applications of Magnetic Materials* (Oxford: Oxford University Press) (<https://doi.org/10.1093/acprof:oso/9780199570447.001.0001>)
- [36] Engelmann U M, Shasha C, Teeman E, Slabu I and Krishnan K M 2019 Predicting size-dependent heating efficiency of magnetic nanoparticles from experiment and stochastic Néel-Brown Langevin simulation *J. Magn. Magn. Mater.* **471** 450–6
- [37] Jonasson C et al 2019 Modelling the effect of different core sizes and magnetic interactions inside magnetic nanoparticles on hyperthermia performance *J. Magn. Magn. Mater.* **477** 198–202
- [38] (Available at: <https://github.com/jupyterlab/jupyterlab>)
- [39] Kluyver T et al 2016 Jupyter notebooks—a publishing format for reproducible computational workflows, position, power acad. publ. play. agents agendas *Proc. 20th Int. Conf. Electron. Publ. ELPUB 2016* pp 87–90
- [40] Carrey J, Mehdaoui B and Respaud M 2011 Simple models for dynamic hysteresis loop calculations of magnetic single-domain nanoparticles: application to magnetic hyperthermia optimization *J. Appl. Phys.* **109** 083921
- [41] Respaud M 1999 Magnetization process of noninteracting ferromagnetic cobalt nanoparticles in the

- superparamagnetic regime: deviation from Langevin law *J. Appl. Phys.* **86** 556–61
- [42] Khandhar A P, Ferguson R M, Simon J A and Krishnan K M 2012 Tailored magnetic nanoparticles for optimizing magnetic fluid hyperthermia *J. Biomed. Mater. Res. A* **100A** 728–37
- [43] Skomski R 2008 *Simple Models of Magnetism* (Oxford : Oxford University Press)
- [44] Ogawa T et al 2013 Challenge to the synthesis of α'' -Fe₁₆N₂ compound nanoparticle with high saturation magnetization for rare earth free new permanent magnetic material *Appl. Phys. Express* **6** 073007
- [45] Dirba I, Yazdi M B, Radetinac A, Komissinskiy P, Flege S, Gutfleisch O and Alff L 2015 Growth, structure, and magnetic properties of γ' -Fe₄N thin films *J. Magn. Magn. Mater.* **379** 151–5
- [46] Costa-Krämer J L, Borsa D M, García-Martín J M, Martín-González M S, Boerma D O and Briones F 2004 Structure and magnetism of single-phase epitaxial γ' -Fe₄N *Phys. Rev. B* **69** 144402
- [47] Zieschang A M, Bocarsly J D, Dürrschnabel M, Molina-Luna L, Kleebe H J, Seshadri R and Albert B 2017 Nanoscale iron nitride, μ -Fe₃N: preparation from liquid ammonia and magnetic properties *Chem. Mater.* **29** 621–8
- [48] Sakurai M et al 2020 Discovering rare-earth-free magnetic materials through the development of a database *Phys. Rev. Mater.* **4** 114408
- [49] Balasubramanian B, Sakurai M, Wang C-Z, Xu X, Ho K-M, Chelikowsky J R and Sellmyer D J 2020 Synergistic computational and experimental discovery of novel magnetic materials *Mol. Syst. Des. Eng.* **5** 1098–117
- [50] Coey J M D 2012 Permanent magnets: plugging the gap *Scr. Mater.* **67** 524–9
- [51] Hofer L J E and Cohn E M 1959 Saturation magnetizations of iron carbides *J. Am. Chem. Soc.* **81** 1576–82
- [52] Edström A et al 2015 Magnetic properties of (Fe_{1-x}Cox)₂B alloys and the effect of doping by 5d elements *Phys. Rev. B* **92** 174413
- [53] Pal S K, Diop L V B, Skokov K P and Gutfleisch O 2017 Magnetic properties of Mo-stabilized bulk Fe₃B magnet *Scr. Mater.* **130** 234–7
- [54] Coey J M D 2010 *Magnetism and Magnetic Materials* (Cambridge: Cambridge University Press) (<https://doi.org/10.1017/CBO9780511845000>)
- [55] Gonzales-Weimuller M, Zeisberger M and Krishnan K M 2009 Size-dependant heating rates of iron oxide nanoparticles for magnetic fluid hyperthermia *J. Magn. Magn. Mater.* **321** 1947–50
- [56] Meffre A, Mehdaoui B, Kelsen V, Fazzini P F, Carrey J, Lachaize S, Respaud M and Chaudret B 2012 A simple chemical route toward monodisperse iron carbide nanoparticles displaying tunable magnetic and unprecedented hyperthermia properties *Nano Lett.* **12** 4722–8
- [57] Mehdaoui B, Meffre A, Carrey J, Lachaize S, Lacroix L M, Gougeon M, Chaudret B and Respaud M 2011 Optimal size of nanoparticles for magnetic hyperthermia: a combined theoretical and experimental study *Adv. Funct. Mater.* **21** 4573–81
- [58] Dirba I, Komissinskiy P, Gutfleisch O and Alff L 2015 Increased magnetic moment induced by lattice expansion from α -Fe to α' -Fe₈N *J. Appl. Phys.* **117** 173911
- [59] Zhang H, Dirba I, Helbig T, Alff L and Gutfleisch O 2016 Engineering perpendicular magnetic anisotropy in Fe via interstitial nitrogen: n choose K *APL Mater.* **4** 116104
- [60] Chen Y-C et al 2020 Element-resolved study on the evolution of magnetic response in Fe_xN compounds *J. Magn. Magn. Mater.* **498** 166219
- [61] Ji N, Allard L F, Lara-Curzio E and Wang J P 2011 N site ordering effect on partially ordered Fe₁₆N₂ *Appl. Phys. Lett.* **98** 2–5
- [62] Ji N, Osofsky M S, Lauter V, Allard L F, Li X, Jensen K L, Ambaye H, Lara-Curzio E and Wang J P 2011 Perpendicular magnetic anisotropy and high spin-polarization ratio in epitaxial Fe-N thin films *Phys. Rev. B* **84** 1–8
- [63] Dirba I, Mohammadi M, Rhein F, Gong Q, Yi M, Xu B X, Krispin M and Gutfleisch O 2021 Synthesis and magnetic properties of bulk α'' -Fe₁₆N₂/SrAl₂Fe₁₀O₁₉ composite magnets *J. Magn. Magn. Mater.* **518** 167414
- [64] Iga A 1970 Magnetocrystalline anisotropy in (Fe_{1-x}Cox)₂B system *Jpn. J. Appl. Phys.* **9** 415–6
- [65] Jian H, Skokov K P, Kuz'Min M D, Radulov I and Gutfleisch O 2014 Magnetic properties of (Fe,Co)₂B alloys with easy-axis anisotropy *IEEE Trans. Magn.* **50** 1–4
- [66] Edström A et al 2015 Magnetic properties of (Fe_{1-x}Cox)₂B alloys and the effect of doping by 5d elements *Phys. Rev. B* **92** 1–13
- [67] Hall R C 1960 Magnetic anisotropy and magnetostriction of ordered and disordered Cobalt-iron alloys *J. Appl. Phys.* **157** 10–12
- [68] Dirba I, Schwöbel C A, Zintler A, Komissinskiy P, Molina-Luna L and Gutfleisch O 2020 Production of Fe nanoparticles from γ -Fe₂O₃ by high-pressure hydrogen reduction *Nanoscale Adv.* **2** 4777–84
- [69] Hijikata M, Ozawa K and Nakatani I 1993 Iron-nitride magnetic fluids prepared by vapor-liquid reaction and their magnetic properties *J. Magn. Magn. Mater.* **122** 10–14
- [70] Žák T and Jirásková Y 2006 CONFIT: Mössbauer spectra fitting program *Surf. Interface Anal.* **38** 710–4
- [71] Gonser U and Spectroscopy M 1975 *Springer-Verlag Berlin Heidelberg* (Berlin: Springer) (<https://doi.org/10.1007/3-540-07120-2>)
- [72] Gütlisch P, Bill E and Trautwein A X 2011 *Mössbauer Spectroscopy and Transition Metal Chemistry: Fundamentals and Applications* (Berlin: Springer) (<https://doi.org/10.1007/978-3-540-88428-6>)
- [73] Kubániová D, Cesnek M, Milkovi C O, Kohout J and Miglierini M 2016 Composition of α -Fe nanoparticles precipitated from CuFe alloy studied by hyperfine interactions *Hyperfine Interact.* **237** 136
- [74] Menil F 1985 Systematic trends of the 57Fe Mössbauer isomer shifts in (FeOn) and (FeFn) polyhedra. Evidence of a new correlation between the isomer shift and the inductive effect of the competing bond T-X (\rightarrow Fe) (where X is O or F and T) any element with a formal posit *J. Phys. Chem. Solids* **46** 763–89
- [75] Bezdička P, Kláriková A, Paseka I and Závěta K 1998 Magnetic properties of α' -Fe_{Nx} and α'' -Fe₁₆N₂ nitrides *J. Alloys Compd.* **274** 10–17
- [76] Novák P, Štěpánková H, Englich J, Kohout J and Brabers V A M 2000 NMR in magnetite below and around the verwey transition *Phys. Rev. B* **61** 1256–60
- [77] Ximendes E et al 2021 Infrared-emitting multimodal nanostructures for controlled *in vivo* magnetic hyperthermia *Adv. Mater.* **33** 2100077